Limb Compliance for Underactuated Propulsion in Resistive Media

Subin Chae[1], Michael Tolley[1], and Nick Gravish[1]

***Abstract*— Soft robots often use appendages that have distributed and anisotropic compliance which allow bending motions that enable locomotion. Anisotropic compliance is especially important for robots that swim in resistive media like fluids or sand since forward motion relies on anisotropic propulsion forces. In this paper we investigate the role of limb compliance in enabling effective swimming of a two-appendage robot through resistive media. We selected joint stiffness values as limb design parameters and performed numerical optimization using granular Resistive Force Theory (gRFT) to maximize displacement per cycle while minimizing motor cost as approximated by the square of the torque. The optimization reveals that asymmetric joint stiffness and tapered configuration outperform symmetric design or asymmetric design with uniform stiffness. We fabricated the limb with 3D printed appendages: polylactic acid (PLA) links and thermoplastic polyurethane (TPU) joints. We characterized joint stiffness via four-point bending experiments and conducted displacement experiments in glass beads. The results verify that limb compliance affects propulsion performance and motor torque requirements. Also, the body drag and the swimming depth affect the propulsion performance. The study provides guidelines for choosing joint stiffness and robot body drag that increase propulsion while managing reasonable motor torque.**

I. INTRODUCTION

Locomotion of soft bodied systems in resistive media is of significant interest in robotics and biology. Bacteria swimming in viscous fluids, worms wriggling through mud, and snakes burrowing beneath granular media all use compliant body elements to propel themselves forward. Resistive forces like those in fluids and sand are unique because a force on a body element, F, is generated only through the relative motion of that body element through the media, $F = f(\mathcal{V})$. This is in contrast to forces like static friction, or ground contact normal force where no motion is required to generate a force on the body. Thus, in resistive media the motion of a body and the forces exerted on it are intrinsically tied together. In the case of compliant limbs, this feedback coupling between: 1) actuated motion of the appendage, 2) the resistive forces on the compliant elements, and 3) the deformation of the compliant limb, all conspire to make compliant underactuation in resistive media a challenging design case for soft robots.

Building on robotic locomotion theories that treat the ground as a rigid plate, prior terradynamic studies have advanced precision design, mechanism optimization, and control methods [1], [2], [3], [4]. While dry granular media (GM) have been studied, other resistive media remain less explored despite their prevalence and importance. Wet sand, for example, differs from dry sand in that in some cases it can flow like a viscous fluid [5]. Thus, in the case of wet sand, there are two regimes relevant for locomotion: In low-Reynolds-number viscous fluids, inertia is negligible and instantaneous hydrodynamic forces scale linearly with velocity; net locomotion requires non-reciprocal shape changes (as per the Scallop Theorem) [6], [7]. In quasi-static granular media, forces are largely rate-insensitive and depend on geometry, orientation, and depth rather than speed, enabling geometric control of thrust without inertia [2], [8].

Biology motivates compliant appendages in terms of generating net propulsion in resistive media. *Chlamydomonas* cells, a sea alga, generate net thrust using non-reciprocal flagellar waveforms, effectively producing stroke asymmetry between recovery and power phases [7], [9]. Inspired by such strategies, previous robotic work realized "quasi-soft" appendages using rigid underactuated linkages with hard joint limits: joints rotate freely within limits and encounter large effective stiffness at stops to create asymmetric strokes and net propulsive force [10]. Similar to rigid underactuated appendage robots, there have also been trials to leverage the asymmetric compliance of the appendage to dig in the sand [11], [12].

However, unlike *Chlamydomonas* which swims in viscous fluid, a perfectly soft appendage in GM experiences large distributed resistive forces during both recovery and power strokes because granular resistive forces depend on geometry rather than velocity. The speed-dependent force asymmetry exploited in viscous swimming is therefore unavailable in GM, requiring alternative propulsion strategies.

Excess compliance can therefore diminish thrust by yielding the appendage rather than the substrate. This raises a design question: What is the appropriate distribution of joint stiffness in an appendage to maximize forward progress or force economy in granular environments?

Prior work has examined how joint stiffness influences propulsion in both viscous fluids and granular media [13]. Peng *et al.* modeled a single rigid link with a torsional spring at the joint and coupled the kinematics with Resistive Force Theory (RFT) for both media. They optimized the torsional stiffness by maximizing propulsive force, showing that the optimal spring constant differs across media because granular forces are largely rate-insensitive whereas viscous forces scale with velocity. This contrast motivates searching for stiffness levels and distributions tailored to the target medium.

In this paper, we address this question by formulating elastic-joint appendage models with three compliance candidates and associated hypotheses. We link these models

[1]Authors are affiliated with Department of Mechanical and Aerospace Engineering, University of California San Diego, La Jolla, CA 92093 USA {suchae, mttolley, ngravish}@ucsd.edu

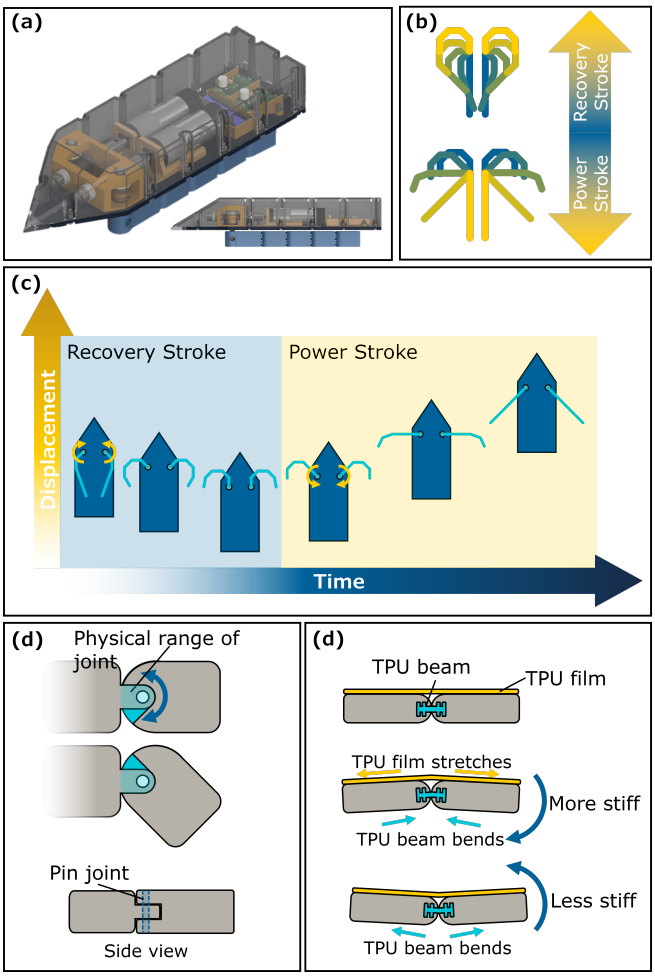

Fig. 1. Design of biologically inspired underactuated compliant limbs for propulsion in granular media. (a) Robot CAD, (b) Concept of asymmetric appendage motion leading to a power and recovery stroke, (c) Concept of the robot propulsion, (d) prior hard-stop underactuated appendage design, (e) soft appendage concept

to resistive force models for viscous and granular media and optimize the joint stiffness and damping parameters under fabrication-feasible bounds. Then we validate the joint stiffnesses with fabricated prototypes whose calibrated joint properties are compared against model predictions. We finally demonstrate the optimized design integrated into a sand-swimming robot. The overall concept of the sand swimming robot is illustrated in Fig. 1.

II. MODELING & OPTIMIZATION

A. Resistive Force Theory

We define resistive media as a continuum environment in which the forces acting on a body, F, are only a function of the relative motion of the body, $F = f(\mathcal{V})$. For example, in 1-D motion in the x-direction of a sphere through a viscous fluid we have the well known Stokes drag law, $F_x = -Cv_x$, where C is a drag coefficient determined by the sphere geometry. Motion of a plate through viscous fluids yields a force-torque body wrench determined by the product of a drag matrix and the body twist, $\mathcal{F}_b = B\mathcal{V}_b$. In more complex resistive media such as dry sand, the relationship between body wrench and body twist is nonlinear, but still solely a function of relative motion $\mathcal{F}_b = f(\mathcal{V}_b)$.

To calculate forces on more complicated shapes beyond flat plates, Resistive force theory (RFT) was developed. RFT is an empirical theory that was originally developed to estimate the forces on objects in low-Reynold's-number fluids [14], and more recently has been extended to other media such as sand [8]. RFT assumes that a complex shape can be broken down into a connected structure of flat plate elements, and that the forces on these flat plates are independent of each other. From this assumption, the net force on an object can be calculated as the sum of the individual forces on the flat plates, which themselves are easily calculated from the resistive media's force law ($\mathcal{F}_b = f(\mathcal{V}_b)$). A further assumption is that the system motion is slow enough so that it remains in the quasi-static regime and the inertial effect in such system is negligible. From these two assumptions, we can generate a quasi-static force balance from the summed RFT elements and solve for the resultant body twist(s) that ensure the quasi-static condition.

Resistive force laws in viscous and granular media show a notable difference: While resistive force in low-Reynolds number fluid is dependent on the velocity (i.e., faster velocities lead to larger resistive forces) the resistive force in granular media is independent of the velocity [15]. In granular media, the magnitude of the velocity does not influence the force on the body (as long as speed remain lower than $\approx$1 m/s). Rather, the geometry of the object and the angle of attack of the object govern the force. This distinction becomes particularly important for robotic locomotion systems that employ rotational appendages for propulsion or maneuvering. For rotational appendages, the force profiles differ significantly between the two media, as illustrated in Fig. 2.

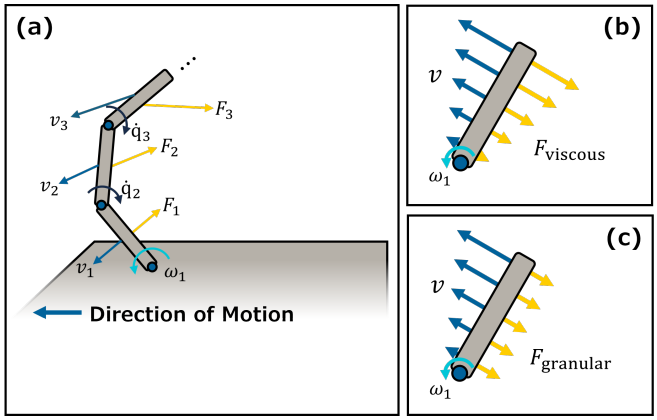

Fig. 2. Concept of appendage swimming and comparison between media. (a) Schematic of the swimming appendage and the key variables. (b) Illustration of appendage motion and corresponding force distribution in a low-Reynolds-number fluid. (c) Illustration of appendage motion and force distribution in granular media, highlighting the velocity independence of resistive force behavior.

B. Appendage Design & Kinematics

We investigated two cases of joint stiffness configurations: symmetric and asymmetric stiffness. For both cases, the joint stiffness was modeled as a linear torsional spring, as illustrated in Fig. 3. Symmetric stiffness applied identical spring constants for positive and negative joint angles about the neutral axis ($0°$), while asymmetric stiffness employs different spring constants for each angular direction (k^+ for positive angles, k^- for negative angles). The appendage geometry is designed as a rectangular beam shape.

Resistive forces in these media are governed by appendage geometry, necessitating careful selection of design parameters including link length, width, and joint stop angle. Among these geometric parameters, we focus on joint stiffness as the primary variable of interest because it influences propulsive force generation through both perpendicular and parallel force components relative to the direction of motion. Other design parameters exhibit more straightforward scaling relationships; for instance, increasing linkage height yields a monotonic increase in generated force. To isolate the geometric effects of joint compliance, we constrain the range of motion to $0 - 180$ degrees and assume, as a simplifying assumption, uniform spring constants and damping coefficients across all limbs. While numerous metrics exist for evaluating locomotion performance, we adopt net displacement as the primary performance measure, which simplifies analysis within the 2D quasi-static framework. In resistive media, achieving positive net displacement in the propulsive direction remains fundamentally challenging and has been a central target in prior studies [10], [16], [17].

Due to the quasi-static nature of the resistive media, displacement is computed by solving the force-equilibrium condition in Eq. 1 to obtain the instantaneous body translation velocity, followed by temporal integration using Implicit Euler method. To model a continuum compliant limb we use a beam-element approximation which consists of a five serial multi-link arm attached to a rigid body. To isolate appendage performance, the body is constrained to translate exclusively along the x-axis through a prismatic degree of freedom (DOF), with lateral (y-direction) motion and rotation prohibited. Resistive forces and torques acting on the arm links are evaluated using granular Resistive Force Theory (gRFT), although only the net x-direction force is of interest for propulsion analysis. The proximal joint is actuated as a motorized revolute joint, while the remaining distal joints are passive revolute joints. We examine the two stiffness cases described previously–symmetric and asymmetric–by applying the respective spring constants to all passive joints, with initial conditions set to joint angle vector $q(0) = 0$ (straight configuration) and body position $x(0) = 0$. Initially, body drag is neglected to isolate the appendage dynamics; the effects of body drag are subsequently examined in the results section.

$$\sum F = F_{\text{body}} + F_{\text{appendage}} \tag{1}$$

For the symmetric stiffness case, joint stiffness is swept

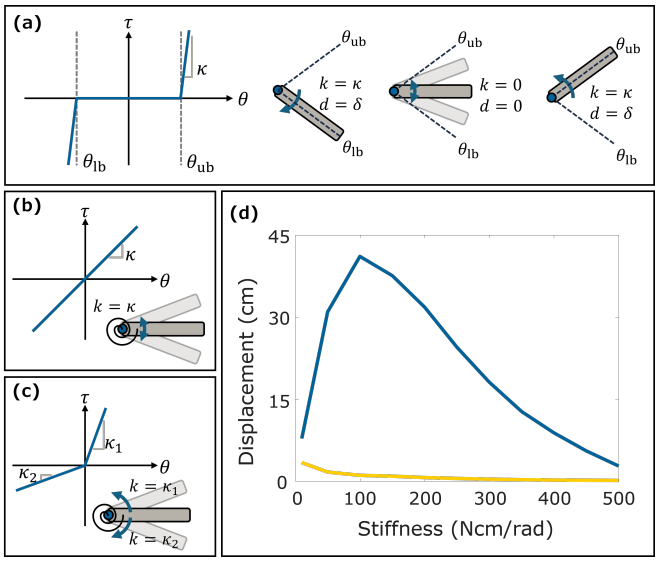

Fig. 3. Three joint-design cases and corresponding torque-angle characteristics and displacement from gRFT simulations for symmetric and asymmetric joint configurations. (a) Hard-stop underactuated joint: free rotation within limits; stiffness rises steeply near the stops to prevent overtravel. (b) Symmetric linear spring: equal stiffness in both directions about the neutral angle. (c) Asymmetric linear torsional spring: different stiffness for clockwise and counterclockwise rotation. Schematics and $\tau(\theta)$ are shown. (d) Net displacement over 10 cycles for different joint stiffness values. The blue curve represents the asymmetric case, and the yellow curve represents the symmetric case.

from 10 N cm/rad (initial value) to 500 N cm/rad in subsequent 50 N cm/rad increments. To reduce sensitivity to initial configuration, net displacement is computed over the first 10 locomotion cycles in MATLAB, where each cycle comprises one recovery stroke and one power stroke. For the asymmetric stiffness case, all joints employ $k^+ = 700$ N cm/rad for positive joint angles and $k^- \in [10, 500]$ N cm/rad for negative joint angles, with k- values spanning the same range as the symmetric case.

C. Stiffness Optimization

As shown in Fig. 3 (d), the symmetric stiffness case exhibits a gradual increase in net displacement with increasing stiffness, though the absolute magnitude remains small. In contrast, the asymmetric stiffness case demonstrates a substantial increase in net displacement up to a critical stiffness k^* (the stiffness yielding maximum net displacement), beyond which performance declines. These results reveal three key insights: (1) symmetric stiffness fails to break the force symmetry in resistive media, resulting in limited net propulsion; (2) for asymmetric stiffness, excessively compliant appendages yield under granular resistive forces during the power stroke, causing the structure to collapse rather than displace the substrate; and (3) overly stiff appendages generate comparable forces during both power and recovery strokes, negating net displacement gains. Consequently, an optimal stiffness region exists that maximizes net displacement.

Having established that joint stiffness significantly influences propulsion, we hypothesized that permitting joint-wise

stiffness variation may yield further performance gains. This hypothesis was motivated by the observation that in rotational appendages, proximal joints experience substantially higher torque loads than distal joints, suggesting that an optimal stiffness distribution should reflect these differential mechanical demands. To investigate this, we formulate a stiffness optimization problem using a Genetic Algorithm (GA) under fixed geometry and link count. The primary objective is to maximize net propulsive displacement per cycle. The fitness function is defined as the net displacement achieved during the third locomotion cycle, which minimizes the influence of initial configuration (all joints start at $0°$). For the symmetric case, the GA optimizes four variables (k for each passive joint; the actuated proximal joint has no passive elastic element) with stiffness bounds $k \in [0, 700]$ N cm/rad. The upper bound of 700 N cm/rad is chosen to provide sufficient stiffness to resist granular drag forces while maintaining joint angles near zero during operation. The lower bound is set to zero, as negative stiffness would be physically unrealizable and impractical to implement. For the asymmetric case, the GA optimizes eight variables (k^+ and k^- for each passive joint) with bounds k^+,$k^- \in [0, 700]$ N cm/rad. Population sizes follow MATLAB's default scaling of $\min(\max(10 \times \text{nvars}, 40), 100)$, yielding 40 individuals for the symmetric case and 80 for the asymmetric case. Termination criteria include a maximum of 200 generations or 120 hours of computation time. All other GA parameters (mutation, crossover) use MATLAB defaults.

As specified previously, optimization was performed for 200 generations, as shown in Fig. 4, yielding optimal stiffness distributions of $k^+ \approx [700, 700, 700, 700]$ N cm/rad and $k^- \approx [700, 47, 28, 12]$ N cm/rad for the four passive joints from proximal to distal. These results indicates that asymmetric stiffness is necessary for generating net propulsion in granular media, as all k^+ values converged to the upper bound provided to the optimizer. The lower bound stiffness exhibits a tapered distribution, decreasing from proximal to distal joints. This distribution aligns with the physical interpretation that torque loads imposed by granular resistance are highest at proximal joints, which support the cumulative reaction forces from all distal segments, and decrease toward the distal end where each joint experiences only local forces. To prevent excessive yielding under these distributed loads, joints near the base require higher stiffness to resist the larger torques they experience.

III. DESIGN & FABRICATION

A. Appendage fabrication

To construct a flexible arm appendage comprising rigid linkages and flexible joints, we fabricated the linkage and joints via 3D printing using Polylactic Acid (PLA) and Thermoplastic Polyurethane (TPU), respectively. The fabrication concept is illustrated in Fig. 5 (a). The primary design parameter is the joint thickness L (measured in the y-direction perpendicular to the bending axis in the xy-plane), which governs joint flexibility. As the joint thickness

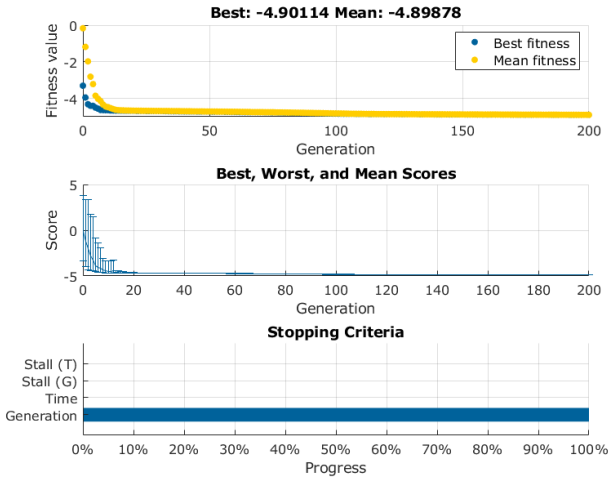

Fig. 4. Genetic Algorithm optimization process showing convergence over 200 generations, with cost function reduction from initial to final values.

increases, the bending stiffness increases, requiring greater moment for the same angular deflection.

To characterize the relationship between joint geometry and rotational stiffness, we conducted four-point bending experiments. The joint stiffness is assumed to be linear within the small-deformation regime, and the specimen is configured as simply supported at both ends. Under four-point bending, the moment between the two inner loading points remains constant, yielding a joint moment $M = \frac{Fa}{2}$, where F is the applied force and a is the distance between the support and loading points, as shown in Fig. 5 (d). From geometric analysis of the deflected configuration, the relative angle θ between adjacent rigid links is calculated as $\theta = 2\arctan(a/d)$, where d is the measured vertical deflection. The rotational stiffness is then determined as expressed in Eq. 2.

$$k_{\text{torsion}} = \frac{Fa}{2(\pi - 2\arctan(a/d))} \tag{2}$$

The TPU joints were printed with Shore hardness 95A, layer height 0.16 mm, and 100% infill (solid walls) to ensure structural uniformity and repeatability. Each geometry was characterized using a single specimen tested three times to verify measurement consistency, yielding stiffness values with coefficient of variation less than 5%, which validated the assumption of high print repeatability. Loading was limited to deflections below 3 mm to maintain the linear elastic regime.

B. Experiment Setup

For the displacement experiment, we employed an air-fluidizable sandboxes to ensure uniform initial compaction of the granular media, as illustrated in Fig. 6. The sandbox was fluidized before each trial and allowed to settle under gravity to achieve consistent loosely packed density [18]. The granular medium consisted of glass beads with particle diameters ranging from 212 to 300μm. To constrain motion

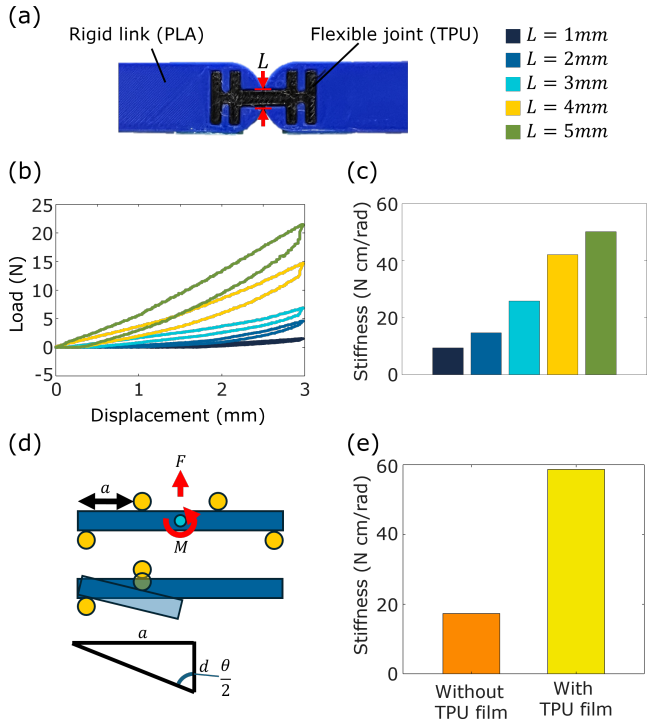

Fig. 5. Concept and characterization of the flexible joint appendage. (a) Material composition and design parameter of the flexible joint. (b) Force−displacement data obtained from the four-point bending experiment (colors correspond to legend in (a). (c) Converted joint stiffness values corresponding to different joint geometries. (d) Schematic illustration of the method used to calculate joint stiffness from the bending experiment. (e) Force difference illustrating the asymmetry induced by attaching a TPU film to one side of the appendage

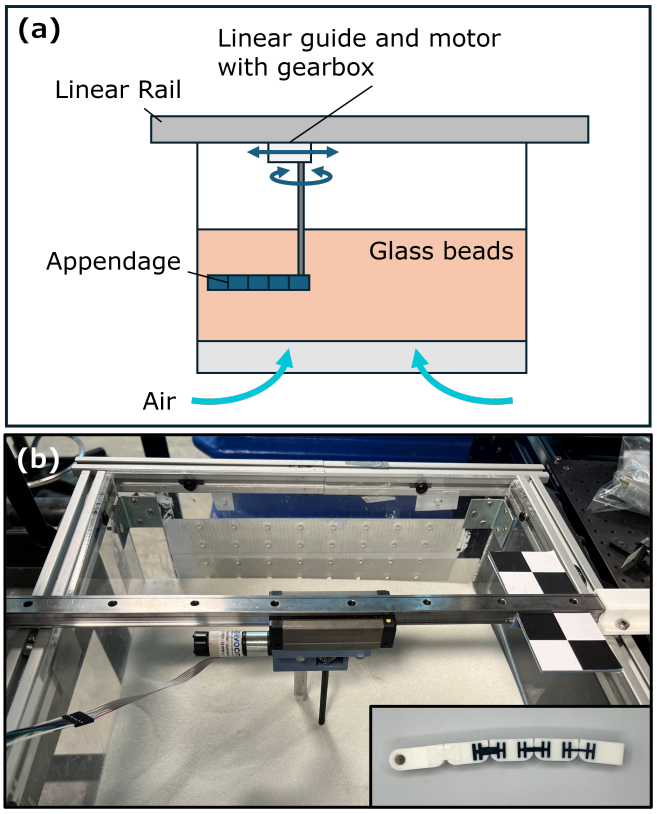

Fig. 6. Experimental setup for displacement measurement. (a) Schematic of the experimental setup used for the displacement experiment. (b) Photo of the setup and the flexible appendage used in the experiment. The checkerboard pattern is employed for 2D camera calibration.

exclusively to the propulsive direction, the motor-appendage assembly was mounted on a linear guide. Note that friction in the linear guide introduces a non-negligible resistance force, the effects of which are discussed in the experimental results section. Displacement data were measured from recorded video (resolution: 1920 × 1080 pixels, frame rate: 30 fps) using the DLTdv digitizing tool[19] with camera calibration performed via checkerboard pattern. Experiments were conducted at a depth of 15 cm measured from the sand surface to the bottom of the appendage, replicating previous sand-swimming robot operating conditions[10]. The proximal joint was actuated by a DC motor operating at 52 RPM under PID control, coupled through a 15:1 worm-worm wheel gear reduction to provide sufficient torque.

IV. RESULTS

A. Joint Stiffness Characterization

We first characterize the rotational stiffness as a function of joint design parameters. Five specimens were fabricated with joint thicknesses $h = 1, 2, 3, 4, 5$ mm. Each specimen was tested three times ($N = 3$ per thickness), yielding standard deviations below 5% for all measurements, which validates the consistency of the 3D printing process and eliminates the need for multiple specimens per geometry. As shown in Fig. 5 (b), (c), peak force and rotational stiffness increases monotonically with joint thickness, demonstrating that joint compliance can be controlled through this single geometric parameter while maintaining all other design parameters, such as material and width, constant.

To assess the predictability of joint stiffness from geometric design, we fit a linear relationship to the measured data, which yielded the best fit among polynomial models tested ($R^2 = 0.93$). Analytical prediction using classical Euler beam theory was not applicable due to the hybrid material composition (PLA and TPU) and the mechanical coupling between the rigid linkages and flexible joint. We chose to build joints with stiffness values of approximately 47, 28, and 12 N cm/rad in accordance with the optimization results.

The fitted curve yielded joint thicknesses of 4.7, 3.0, and 1.5 mm to achieve the target stiffness values, respectively. The experimental characterization of the fabricated joints showed stiffness values of 48.5, 24.3, and 10.9 N cm/rad, corresponding to relative errors of 3.09%, 13.25%, and 9.33% with respect to the target values, respectively. These results demonstrate acceptable agreement and validate that joint stiffness can be reliably controlled through geometric design within engineering tolerances.

Additionally, asymmetric stiffness behavior was characterized by attaching a TPU film (nominal thickness 0.0015 inches, tensile strength $> 8,000$ psi, elongation $> 500\%$)

between adjacent rigid links on one side using cyanoacrylate adhesive (Loctite 495). When the joint bends in the direction that stretches the film, tensile forces in the TPU film provide additional resistance, creating directional stiffness asymmetry. However, for the experimental implementation, the high-stiffness direction ($k^+ \cong 700$ N cm/rad from optimization) was instead achieved through geometric constraints: the rigid linkages were designed with physical stops to prevent rotation beyond $0°$, effectively creating infinite stiffness in that direction. This design choice was motivated by the optimization results indicating that any stiffness exceeding 700 N cm/rad provides sufficient resistance to granular forces, making a physical constraint a practical and robust implementation. The stiffness characteristics for symmetric and asymmetric configurations are presented in Fig. 5 (e), contrasting the behavior with and without TPU film reinforcement on one side of the joint.

B. Torque Cost Analysis

To evaluate the trade-off between propulsive performance and actuation cost, we use the cycle-averaged squared motor torque, $\langle \sum T^2 \rangle$, computed over ten complete cycles. Motor torque is proportional to current ($T = K_t I$), and the dominant copper loss scales with I^2R. Substituting the torque–current relation yields $P_{\text{cu}} \propto T^2$, such that squared torque provides a physically motivated proxy for electrical and thermal actuator burden.

For dimensionless comparison relative to prior work, we normalize both displacement and torque cost by the configuration used in [10], corresponding to a hard-stop joint with $\theta_{\text{low}} = -45°$.

Fig. 7 (a) shows results for the hard-stop appendage with varying minimum joint angle constraints (lower bound θ_{min} preventing joint closure). As θ_{low} decreases from $0°$, net displacement initially increases along with actuator loading. Performance peaks near $\theta_{\text{min}} \approx -30°$, beyond which further restriction yields diminishing displacement gains despite continued increases in torque cost. This indicates an "inefficiency region" where tighter joint constraints demand higher actuation cost without commensurate propulsion benefits.

Fig. 7 (b) presents results for flexible appendage with lower-bound stiffness k^- while maintaining $k^+ = 700$ N cm/rad. The case $k^- = 100$ N cm/rad achieves maximum normalized displacement, with performance degrading as k^- increases. Comparing optimal configurations from both approaches reveals flexible appendages achieve comparable or greater transport ($\Delta x/\Delta x_{\text{ref}} \approx 1.16$ at $\langle \sum T^2 \rangle / \langle \sum T^2_{\text{ref}} \rangle \approx 1.09$) while requiring about 23% lower mean squared torque compared to hard-stop configurations ($\Delta x/\Delta x_{\text{ref}} \approx 1.15$ at $\langle \sum T^2 \rangle / \langle \sum T^2_{\text{ref}} \rangle \approx 1.42$). Furthermore, actuator torque demand increases monotonically with reduced joint mobility in both implementations—either through tighter angular limits (increasing θ_{min}) or increased stiffness (increasing k^-).

This trend reveals that restricting appendage deflection, regardless of implementation method, imposes higher energetic costs on the actuator. The superior efficiency of compliant joints likely results from passive energy storage and return during cyclic motion, reducing the net work required from the actuator.

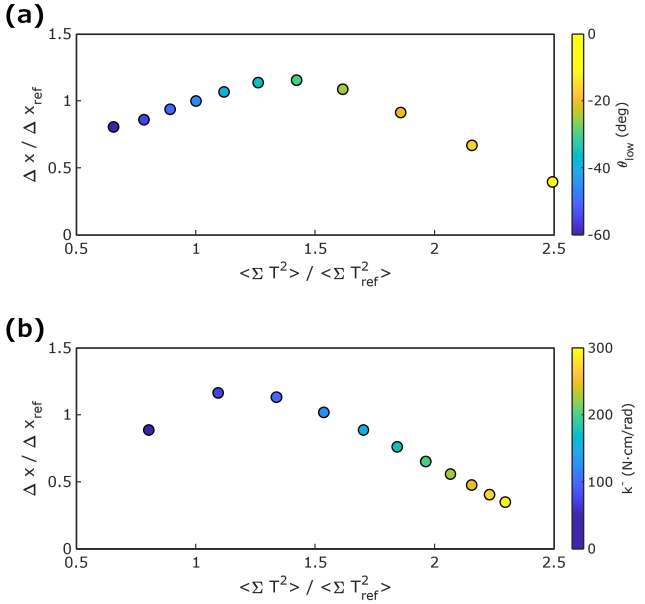

Fig. 7. Torque requirements under different joint configurations. (a) Displacement vs mean torque squared data. The color bar indicates the lower bound of joint angle limits. (b) Displacement vs mean torque squared data. The color bar indicates the lower joint stiffness values.

C. Effect of Body Drag on Propulsion

Body drag significantly influences net propulsive displacement and interacts with joint stiffness optimization. In the simulation, body drag is modeled as Coulomb friction with magnitude $F_{\text{body}} = 11$ N, derived from prior sand-swimming robot studies[10] but reduced by half (from 22 N) to account for the single-appendage configuration, assuming symmetric bilateral appendages in the referenced robot. This is incorporated into the gRFT simulation through the modified force equilibrium condition $F_{\text{appendage}} + F_{\text{body}} = 0$.

Fig. 8 (a) compares net displacement versus joint stiffness for cases with and without body drag, respectively. In the no-body-drag case, maximum displacement occurs at asymmetric stiffness ($k^+ = 700$ N cm/rad, $k^- = 100$ N cm/rad). While the with-body-drag case exhibits qualitatively similar trends, detailed examination of the low k^- region reveals a shift in optimal stiffness: the peak occurs at $k^- = 80$ without body drag, compared to $k^- = 75$ with body drag. This reveals a non-monotonic relationship: an optimal body drag magnitude exists that maximizes net displacement. This demonstrates that optimal joint compliance depends on the magnitude of resistive forces acting on the body.

Counterintuitively, Fig. 8 (a) exhibits larger net displacement for the with-body-drag case in certain parameter regimes—unexpected because body drag is typically detrimental to locomotion. This behavior arises from a force-threshold mechanism: in the with-body-drag case, the appendage only translates forward when instantaneous propulsive forces exceed F_{body}, resulting in reduced forward

displacement per stroke. However, backward displacement during the recovery stroke is similarly constrained.

This threshold behavior is clearly visible in Fig. 8 (b) and (c), where forward motion initiates only when instantaneous propulsive force exceeds F_{body} (indicated by the dashed line). For Fig. 8 (b), we fixed the joint stiffness $k_{\text{high}} = 700$ N cm/rad and $k_{\text{low}} = 100$ N cm/rad and systematically varied the body drag to isolate the pure effect of body drag magnitude independent of stiffness optimization. The net effect is that moderate body drag can suppress detrimental backward displacement more effectively than it penalizes forward propulsion, yielding an optimal drag magnitude of approximately $F_{\text{body}} \approx 10$ N for the tested configuration.

While body drag magnitude is primarily determined by environmental conditions and body cross-sectional area, this finding provides a practical design guideline: robot body geometry should be optimized not to minimize drag unconditionally, but rather to achieve a moderate drag level that balances forward propulsion with backward slip suppression. This suggests that frontal area could be deliberately designed to approach the optimal drag regime identified in simulation.

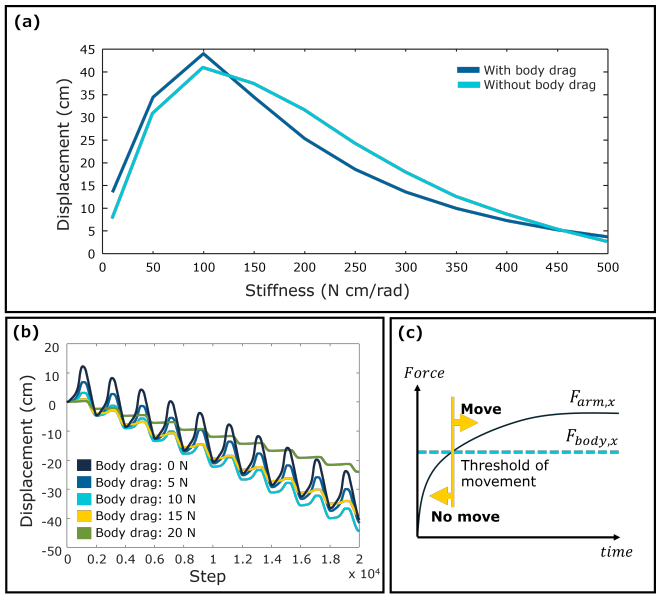

Fig. 8. Effect of body drag on propulsion performance. (a) Simulated displacement over 10 cycles as a function of k^- without body drag. (b) Simulated displacement over 10 cycles as a function of k^- with body drag included. (c) Displacement in the propulsive direction over time for different body drag magnitudes. (d) Schematic illustration explaining how body drag can, in some cases, assist propulsion by generating net forward displacement.

D. Displacement Experiment

We compared optimal and suboptimal appendage configurations across varying body drag and depth. Fig. 9 (a) shows displacement versus body drag for both configurations, while Fig. 9 (b) presents depth effects mapped from the reference depth of 15 cm using the relationship $F_{\text{targetZ}} = sF_{\text{referenceZ}}$ when $s = z_{\text{target}}/z_{\text{reference}}$. With the same body drag, the total displacement of suboptimal case underperforms compared to

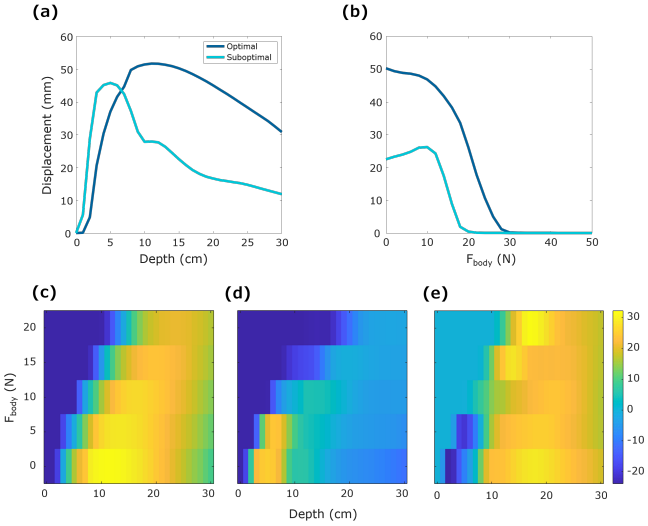

Fig. 9. Body drag and depth effects on net displacement for optimal and suboptimal appendage configurations. (a) Net displacement versus swimming depth at no body drag (b) Net displacement versus body drag at fixed depth at 15 cm (c) Displacement contour map across body drag and depth parameter for the optimal configuration (d) Displacement contour map for suboptimal configuration (e) Difference map (optimal minus suboptimal). Blue regions indicate parameter combinations where the suboptimal configuration outperforms the optimal design.

the optimal case. However, certain depth regimes exist where the suboptimal configuration achieves superior performance, suggesting depth-dependent optimal stiffness.

Fig. 9 (c-e) illustrates the combined effects of body drag and depth variation. The contour plots in Fig. 9(c, d) reveal distinct displacement distributions between optimal and suboptimal configurations. Notably, Fig. 9(e) identifies parameter regions, colored as blue, where the suboptimal configuration outperforms the optimal design, indicating that optimal stiffness distributions are couples to both body geometry and operating depth.

Experimental displacement measurements are presented in Fig. 10 (a) for optimal and suboptimal configurations tested without an attached body. As expected from the optimized tapered design, the optimal appendage exhibits larger excursions in both forward and backward directions compared to the uniform-stiffness case. However, net displacement over multiple cycles shows quantitative disagreement with simulation predictions, Fig. 10 (b).

Several factors likely contribute to this discrepancy. First, experimental constraints introduce non-negligible friction from the linear guide, which was not modeled in simulation. Second, gRFT coefficients calibrated at 15 cm depth may not fully capture force variations across the entire stroke trajectory. Third, the gRFT framework treats each linkage as an isolated force element, neglecting hydrodynamic-like interactions between adjacent links – an assumption that breaks down in dense granular media where previously disturbed regions exhibits altered resistance. Fourth, material nonlinearity in TPU joints under large deformations may deviate from the assumed linear stiffness model. Finally,

small per-cycle displacement errors accumulate over multiple cycles, amplifying the simulation-experiment gap. Future work will address these limitations through improved experimental apparatus and refined modeling approaches.

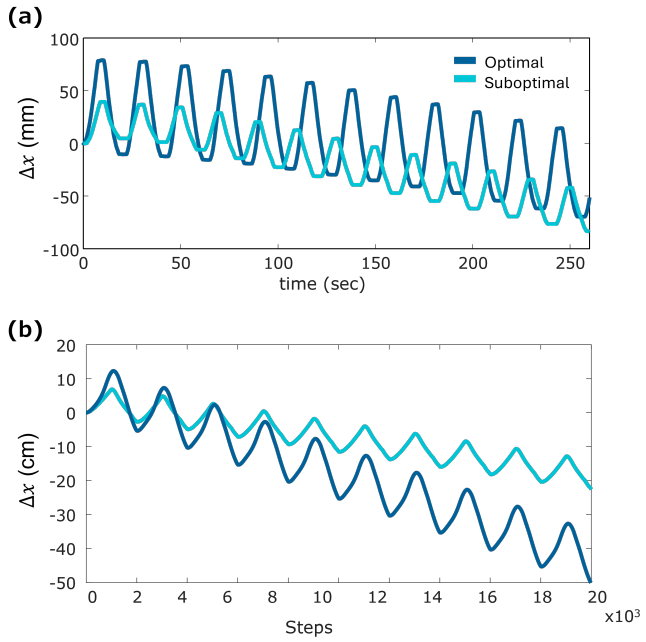

Fig. 10. Displacement trajectories comparing optimal and suboptimal appendage configurations. (a) Experiment results from video tracking, (b) gRFT simulation predictions.

V. CONCLUSION

In this paper, we investigated flexible appendages for granular media propulsion, focusing on joint compliance and body drag effects. Using gRFT simulations, we demonstrated that discretized flexible appendages generate net propulsion through asymmetric stroke kinematics, with joint-wise stiffness optimization via GA significantly enhancing performance. Asymmetric stiffness ($k^+ \neq k^-$) achieved substantially greater displacement than symmetric designs, while compliant joints delivered comparable propulsion with approximately 26% lower actuation torque compared to hard-stop appendages.

Counterintuitively, we identified an optimal body drag magnitude where moderate resistance suppressed backward motion more effectively than it penalizes forward propulsion, suggesting body cross-sectional area should be designed for optimal drag. Experimental validation using 3D-printed appendages with characterized stiffness ($k \propto h$, $R^2 = 0.93$) in air-fluidized glass beads showed $\Delta x \approx 5.7$ cm which was approximately seven times lower than the simulation prediction. Discrepancies are attributed to the empirical limitations of the gRFT model, granular packing heterogeneity, particle slip, nonlinearity of TPU material and linear guide friction.

Future work could refine gRFT calibration across multiple depths, reduce experimental friction, incorporate material nonlinearity, and explore multi-appendage configurations with closed-loop control for robust locomotion across varying substrates.

ACKNOWLEDGMENT

This material is based upon work supported by the Office of Naval Research (ONR) under Grant Nos. N00014-23-1-2358 and N00014-23-1-2169. Any opinions, findings, and conclusions or recommendations expressed in this material are those of the author(s) and do not necessarily reflect the views of the ONR.

REFERENCES

[1] Q. Yu, C. Pavlov, W. Kim, and A. M. Johnson, "Modeling wheeled locomotion in granular media using 3d-rft and sand deformation," *Journal of Terramechanics*, vol. 115, p. 100987, 2024.

[2] C. Li, T. Zhang, and D. I. Goldman, "A terradynamics of legged locomotion on granular media," *science*, vol. 339, no. 6126, pp. 1408–1412, 2013.

[3] F. Qian and D. E. Koditschek, "An obstacle disturbance selection framework: emergent robot steady states under repeated collisions," *The International Journal of Robotics Research*, vol. 39, no. 13, pp. 1549–1566, 2020.

[4] C. Cao, D. Moon, C. Creager, D. K. Lieu, and H. S. Stuart, "Push-pull locomotion: Increasing travel velocity in loose regolith via induced wheel slip," *Journal of Terramechanics*, vol. 110, pp. 87–99, 2023.

[5] M. Macaulay and P. Rognon, "Viscosity of cohesive granular flows," *Soft matter*, vol. 17, no. 1, pp. 165–173, 2021.

[6] E. M. Purcell, "Life at low reynolds number," in *Physics and our world: reissue of the proceedings of a symposium in honor of Victor F Weisskopf*. World Scientific, 2014, pp. 47–67.

[7] E. Lauga and T. R. Powers, "The hydrodynamics of swimming microorganisms," *Reports on progress in physics*, vol. 72, no. 9, p. 096601, 2009.

[8] R. D. Maladen, Y. Ding, C. Li, and D. I. Goldman, "Undulatory swimming in sand: subsurface locomotion of the sandfish lizard," *science*, vol. 325, no. 5938, pp. 314–318, 2009.

[9] S. G. Pozveh, A. J. Bae, and A. Gholami, "Resistive force theory and wave dynamics in swimming flagellar apparatus isolated from c. reinhardtii," *Soft matter*, vol. 17, no. 6, pp. 1601–1613, 2021.

[10] S. Chopra, D. Vasile, S. Jadhav, M. T. Tolley, and N. Gravish, "Toward robotic sensing and swimming in granular environments using underactuated appendages," *Advanced Intelligent Systems*, vol. 5, no. 8, p. 2200404, 2023.

[11] R. A. Russell, "Crabot: A biomimetic burrowing robot designed for underground chemical source location," *Advanced Robotics*, vol. 25, no. 1-2, pp. 119–134, 2011.

[12] D. Li, S. Huang, Y. Tang, H. Marvi, J. Tao, and D. M. Aukes, "Compliant fins for locomotion in granular media," *IEEE Robotics and Automation Letters*, vol. 6, no. 3, pp. 5984–5991, 2021.

[13] Z. Peng, Y. Ding, K. Pietrzyk, G. J. Elfring, and O. S. Pak, "Propulsion via flexible flapping in granular media," *Physical Review E*, vol. 96, no. 1, p. 012907, 2017.

[14] J. Gray and G. J. Hancock, "The propulsion of sea-urchin spermatozoa," *Journal of Experimental Biology*, vol. 32, no. 4, pp. 802–814, 1955.

[15] T. Zhang and D. I. Goldman, "The effectiveness of resistive force theory in granular locomotion," *Physics of Fluids*, vol. 26, no. 10, 2014.

[16] H. C. Astley, J. R. Mendelson III, J. Dai, C. Gong, B. Chong, J. M. Rieser, P. E. Schiebel, S. S. Sharpe, R. L. Hatton, H. Choset *et al.*, "Surprising simplicities and syntheses in limbless self-propulsion in sand," *Journal of Experimental Biology*, vol. 223, no. 5, p. jeb103564, 2020.

[17] D. Ortiz, N. Gravish, and M. T. Tolley, "Soft robot actuation strategies for locomotion in granular substrates," *IEEE Robotics and Automation Letters*, vol. 4, no. 3, pp. 2630–2636, 2019.

[18] N. Gravish, P. B. Umbanhowar, and D. I. Goldman, "Force and flow transition in plowed granular media," *Physical review letters*, vol. 105, no. 12, p. 128301, 2010.

[19] T. L. Hedrick, "Software techniques for two-and three-dimensional kinematic measurements of biological and biomimetic systems," *Bioinspiration & biomimetics*, vol. 3, no. 3, p. 034001, 2008.